

The scaling of proton energies in ultrashort pulse laser plasma acceleration

This article has been downloaded from IOPscience. Please scroll down to see the full text article.

2010 New J. Phys. 12 045015

(<http://iopscience.iop.org/1367-2630/12/4/045015>)

View [the table of contents for this issue](#), or go to the [journal homepage](#) for more

Download details:

IP Address: 129.104.100.20

The article was downloaded on 14/09/2010 at 16:24

Please note that [terms and conditions apply](#).

The scaling of proton energies in ultrashort pulse laser plasma acceleration

K Zeil, S D Kraft, S Bock, M Bussmann, T E Cowan, T Kluge, J Metzkes, T Richter, R Sauerbrey and U Schramm¹

Research Center Dresden-Rossendorf (FZD), PO Box 510119, 01314 Dresden, Germany

E-mail: u.schramm@fzd.de

New Journal of Physics **12** (2010) 045015 (16pp)

Received 8 December 2009

Published 30 April 2010

Online at <http://www.njp.org/>

doi:10.1088/1367-2630/12/4/045015

Abstract. This paper presents a systematic investigation of an ultrashort pulse laser acceleration of protons that yields unprecedented maximum proton energies of 17 MeV at a table-top Ti:sapphire laser power level of 100 TW. For plain few-micron-thick foil targets, a linear scaling of the maximum proton energy with laser power is observed and this is attributed to the short acceleration period close to the target rear surface. Although excellent laser pulse contrast was available, slight deformations of the target rear were found to lead to a predictable shift of the direction of the energetic proton emission away from the target normal that could be used for better discrimination of the low-energy part of the spectrum.

Contents

1. Introduction	2
2. Experimental setup	3
3. Proton energy scaling	4
4. Proton acceleration from foil targets distorted by shock waves	9
4.1. Modeling of the target deformation	11
4.2. Particle-in-cell (PIC) simulation	13
5. Conclusions	14
References	15

¹ Author to whom any correspondence should be addressed.

1. Introduction

In recent years, a number of applications of laser-accelerated ion pulses have been realized or proposed that make use of their unique properties. The high beam-optical quality [1] of particle beams accelerated from the rear side of a laser-irradiated thin foil and the inherent synchronization suggest their use as probes for electric fields in laser-driven inertial confinement fusion [2] and in relativistic laser plasma research [3, 4]. Here, the large energy bandwidth of the non-relativistic particles even allows for improved time mapping by the correlation between time-of-flight and energy. The high charge of the pulses combined with the excellent transverse emittance further motivates the injection of laser-accelerated bunches into synchrotrons after an appropriate phase rotation has been performed [5, 6].

Medical applications, especially in radiation therapy [7], could also take advantage of the broader energy bandwidth, provided that it can be reproducibly matched to the energy loss in a macroscopic target volume. Radiation therapy, however, requires proton energies of up to 250 MeV at a dose rate of a few Gy per minute, and thus a pulse repetition rate of the order of 1 Hz. Although the radiation doses available in single pulses seem promising for use in this field, the average achievable current, and thus the pulse repetition rate, still has to be improved. The crucial and still unresolved issue, however, for most applications is the increase in maximum particle energy. At present, the maximum proton energies achieved with high-energy high-power lasers operating in single pulse mode range between 50 and 60 MeV (for references, see section 3), while with table-top lasers that, in contrast, operate with repetition rates of 10 Hz, energies of only around a few MeV have been reported.

With the recent development of 100 TW class Ti:sapphire lasers with ultrashort pulses with pulse lengths around 30 fs, introduced in section 2, the hope is to bridge the hitherto huge discrepancy in the achievable maximum ion energies between single-shot and table-top laser systems [8, 9]. Systematic studies can now be performed and scaling laws for the most established ion acceleration regime, the target normal sheath acceleration (TNSA) [10], are to be deduced with ultrashort pulses for the identification of feasible routes toward high proton energies at reasonable pulse repetition rates.

In this work, we aim for a simple and robust approach that, following the systematic studies presented in sections 3 and 4, can be developed into a stable proton source operating at high repetition rates. Thus, micron-thick plain metal foils were used as targets that can later be operated, e.g. in tape targets, although more complex structured or mass-limited targets are promising candidates for further improvement of the spectral quality [11] and of the maximum energies [12]. With the 150 TW laser Draco (Dresden laser acceleration source), recently installed at the research center Dresden–Rossendorf (FZD), we were able to demonstrate the highest proton energies observed so far with a 10 Hz repetition rate table-top laser system, and could show a strong deviation from the well-known square-root scaling of the proton energy with laser power to a linear scaling. After a revision of the existing analytical models for the scaling of maximum energies, we derive that the measurement can be well explained in the frame of these models, a fact that has not been discussed so far to our knowledge. Furthermore, we present in section 4 that the detection of the maximum proton energy can be complicated by a preplasma-induced deformation of the foil, even for state-of-the-art laser pulse contrast. This effect is experimentally well known [13] for 10 TW class lasers and can be qualitatively explained analytically as well as in two-dimensional (2D) particle-in-cell (PIC) simulations for the parameters of the experiment. As the experimental results strongly rely on the laser

parameters on the target, the following section is devoted to a detailed technical description of the experiment, which may serve as a reference for the emerging class of 100 TW lasers.

2. Experimental setup

The experiments were performed with the ultrashort pulse 150 TW laser system Draco, recently installed at the research center Dresden–Rossendorf. Based on the Pulsar design of Amplitude Technologies (France) [14], the chirped pulse amplification Ti:sapphire system consists of a regenerative amplifier and three stages of multipass amplifiers capable of delivering up to 6 J pulse energy at a pulse repetition rate of 10 Hz. Cryogenic cooling in the last amplifier ensures a stable beam profile for single pulse operation, as well as for variable pumping power, and thus variable beam energy. Spectral gain narrowing in the amplifier chain is pre-compensated for by an acousto-optic filter inside the cavity of the regenerative amplifier (Mazzler, Fastlite). Active control of spectral losses allows for a full amplification bandwidth of up to 80 nm and thus pulse durations of below 25 fs after compression. An independent second programmable acousto-optic filter (Dazzler), controlling the spectral phase of the pulse, is used in combination with a SPIDER (APE) diagnostic of the compressed pulse for the pre-compensation of higher order dispersion effects in the chain. Following compression, wavefront corrections are performed with a large aperture deformable mirror imaged onto a wavefront sensor (Phasics) and potential pulse-front tilts are interferometrically monitored and minimized over the full aperture [15].

For the first series of experiments discussed here, the laser pulse is transported into a dedicated target area with an overall efficiency (compared to the energy level directly behind the last amplifier) of about 60%. The wavefront corrected beam of about 90–100 mm diameter is tightly focused using an off-axis parabolic mirror with a focal length of 250 mm to a spot size of about 3 μm diameter (full-width at half-maximum, FWHM). About 80% of the laser energy can be concentrated inside the focal spot, as shown by the enlarged image in figure 1. Hence, peak intensities exceeding $10^{21} \text{ W cm}^{-2}$ are readily achieved on the target. The parameters, which have routinely been achieved on the target for experiments, are listed in table 1 and compared with the design parameters of the system.

Special measures are taken to optimize the temporal pulse contrast of the system. By means of two saturable absorbers, one cleaning the short energy boosted oscillator pulse at a pulse duration of a few ps and the other installed behind the regenerative amplifier, the amplified spontaneous emission (ASE) background from both cavities is significantly suppressed. Measurements with a high dynamic range third-order autocorrelator (Sequoia, Amplitude Technologies), depicted in figure 2, show that a level pulse contrast ratio of few 10^{-10} can be achieved over several 100 ps before the intensity starts to increase about 30 ps ahead of the main pulse. On the ns time scale, the ASE pedestal as well as prepulses leaking out of the regenerative amplifier or originating from cross-talk in the multipass amplifiers are measured with a fast photodiode (rise time of 1 ns) using calibrated absorption filters and a fast oscilloscope. The ASE signal begins to become measurable about 3.5 ns before the main pulse and reaches an energy contrast which, integrated over 100 fs (time resolution of the third-order autocorrelator), is consistent with the intensity contrast measurement for a few 100 ps. This is achieved by means of two pulse cleaning Pockels cells, one of which also protects the laser front-end against target back reflections.

As sketched in figure 3, thin metal foil targets are irradiated with p-polarized light at an incident angle of $\phi = 45^\circ$. Positioning in the focal plane is continuously monitored between

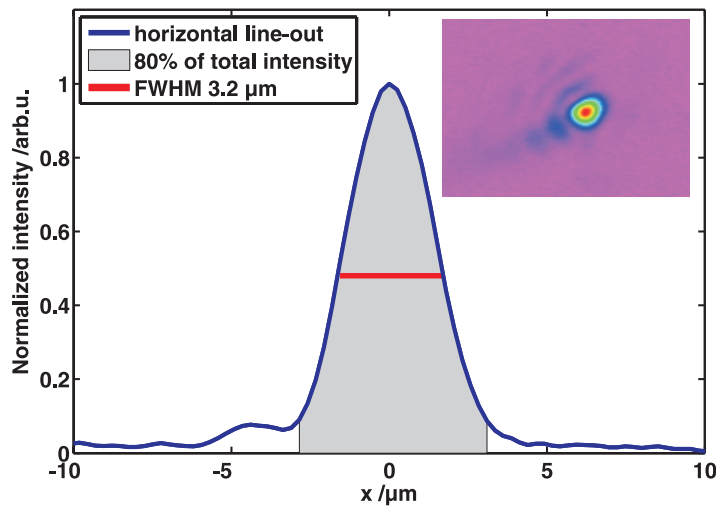


Figure 1. Enlarged image of the focal spot measured inside the target chamber (inset, linear rainbow color scale) where the dynamic range in the wings is increased by multiple exposure techniques using calibrated attenuators. The diameter (FWHM) of the spot amounts to $3.2 \mu\text{m}$ in the horizontal and $2.8 \mu\text{m}$ in the vertical, respectively, which is due to a slight ellipticity in the incoming beam. The horizontal line out illustrates that 80% of the laser energy can be found inside the focal spot.

consecutive laser shots by backside imaging, as well as front-side imaging of the focal spot of an alignment laser beam exactly copropagating with the high-power beam, resulting in an alignment precision for the focus depth of $10 \mu\text{m}$. Proton pulses emitted from the target rear side under the target normal direction are detected using stacks of radiochromic film (RCF) dosimetry media and under the target normal using a Thomson parabola spectrometer with an entrance aperture of $0.25 \mu\text{sr}$. With RCF the spatial distribution of the proton fluence can be measured. Moreover, stacking of many RCF slices provides a coarse energy resolution due to the range–energy relationship of the stopping power. From the RCF data, the proton spectrum can be reconstructed, and since the complete proton beam can be recorded, a calculation of the conversion efficiency of laser to total proton energy is possible [16]. In this study, stacks of GafChromic EBT films covered with $13 \mu\text{m}$ Al foil are used. The RCF stacks are mounted on a motorized wheel in order to irradiate at least eight stacks before opening the target chamber becomes necessary. For the detection of the proton spectra with higher spectral resolution and to distinguish different ion species, a Thomson parabola spectrometer consisting of parallel magnetic (560 mT) and electric fields ($3.7 \times 10^5 \text{ V m}^{-1}$) is used. The parabolic ion traces are recorded using a multi-channel plate with the phosphor anode imaged to a 12-bit CCD camera in order to provide online analysis of the obtained ion spectra in the energy range of 1–30 MeV.

3. Proton energy scaling

Over the last decade, maximum proton energies well above 10 MeV could only be observed when high-power high-energy lasers were applied for the irradiation of thin foils, as summarized by the open circles in figure 4. At the same time, maximum energies reached with short pulse

Table 1. Comparison of the design parameters of the 150 TW Draco system and those reproducibly achieved during the first experimental campaign. All parameters refer to conditions on target. The intensity is derived using a focal spot diameter (FWHM) of $3\ \mu\text{m}$. Contrast is given as the power ratio with reference to the maximum pulse power, as discussed below.

Parameters	E_L (J)	τ (fs)	Strehl ratio	Intensity (W cm^{-2})	Picosecond contrast	Prepulse contrast
Design	4	23–30	0.3	$>10^{21}$	10^{-10}	$<10^{-7}$
Experiment	3	30	>0.9	$>10^{21}$	5×10^{-9}	$<10^{-9}$

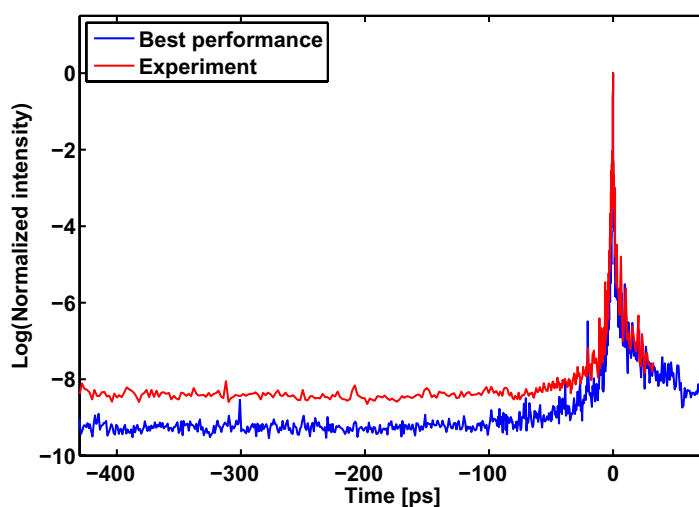


Figure 2. Measured laser pulse contrast on the ps to a few 100 ps time scale. Comparison of a best performance curve with the conditions measured during the experiments presented in this paper.

lasers were generally limited to only a few MeV, as illustrated by the colored diamonds where the color represents the typical ranges of pulse durations of such lasers of $\tau_1 = 30, \dots, 100$ fs. While for the aforementioned long-pulse high-power lasers with $\tau_1 \gg 100$ fs, a clear scaling of the maximum proton energies with the square root of the laser power could be established experimentally [8], no obvious dependence could be obtained from the short pulse laser data, this having been partly due to the fact that these sub-10 TW lasers were operating close to the MeV proton energy threshold. As reported in the following, this situation has changed with the recent advent of 100 TW class ultrashort pulse lasers ($\tau_1 \sim 30$ fs).

The red squares in figure 4 represent the results from our systematic studies where the laser energy has been varied while keeping its pulse duration and focusing parameters constant. Maximum proton energies of up to 17 MeV have been reached and have thus considerably extended the energy range accessible with compact ultrashort pulse laser systems. Moreover, the scaling of the maximum proton energy with laser power has been found to significantly deviate from the well-established square-root scaling. This novel scaling regime, exhibiting a faster linear scaling with laser power for ultrashort laser pulses, can be basically understood as

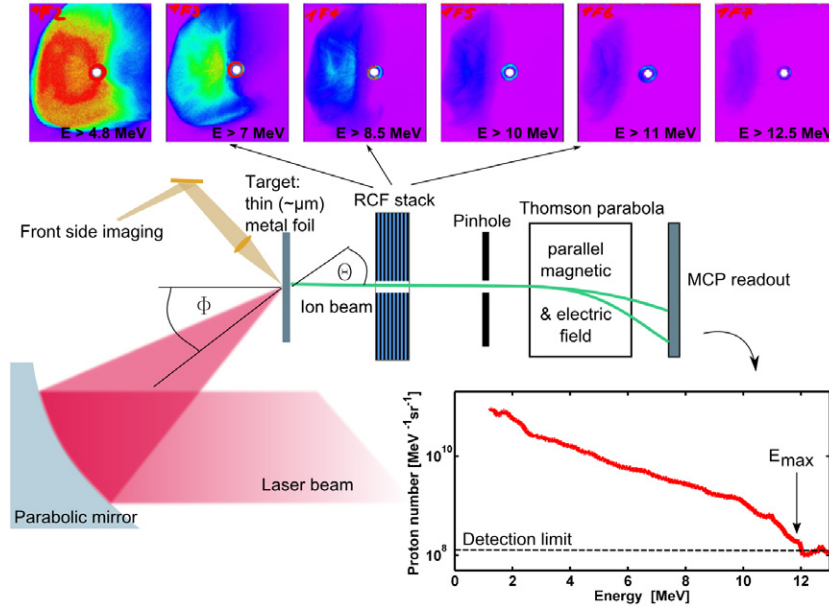


Figure 3. Schematic overview of the experimental setup and the proton diagnostics used in the present experiments. ϕ represents the incident angle of the laser with respect to the target normal direction and θ refers to the proton emission angle from the back surface of the target foil with respect to the target normal. The complete proton beam is detected with RCF stacks positioned at about 50 mm behind the target and, through a hole in the center of the RCF stack, the proton spectrum is measured with a Thomson parabola spectrometer for a small solid angle in the target normal direction. An RCF stack sample trace is displayed as a false color image (top). A similar spectrum recorded with the magnetic spectrometer shows a typical proton spectrum with a cut-off energy of 12 MeV (bottom).

a consequence of the 3D field distribution in the vicinity of the target rear surface. For the sake of simplicity, the analytical model of Schreiber *et al* [9] will be used in a novel interpretation to illustrate the transition between the two regimes.

The model is based on the assumption that a relativistic laser pulse of pulse duration τ_1 accelerates N_e electrons from the target front side to an average energy E_e . The total number of electrons is determined by the efficiency η of the conversion of laser energy E_1 into electron energy $N_e E_e = \eta E_1$. The electron bunch of length $\tau_1 c$ leaves the target rear side spread to a circular area of radius $R = r_1 + d \tan \vartheta$, where r_1 denotes the radius of the laser focal spot, d the thickness of the irradiated thin foil and ϑ the half-angle of the propagation cone. As a consequence, a positive surface charge $Qe/(\pi R^2)$ is induced at the rear side of the target. It leads to the on-axis potential distribution

$$\Phi(r=0, \zeta) = -\frac{Qe}{2\pi\epsilon_0 R} \left(1 + \zeta - \sqrt{1 + \zeta^2}\right), \quad (1)$$

where $\zeta = z/R$ stands for the normalized propagation direction normal to the foil. Electrons of average energy E_e are forced to turn around at a distance $\zeta_t = E_e/E_\infty$ assuming $\zeta_t \ll 1$. The equation of the equilibrium number of electrons outside of the foil with the induced surface

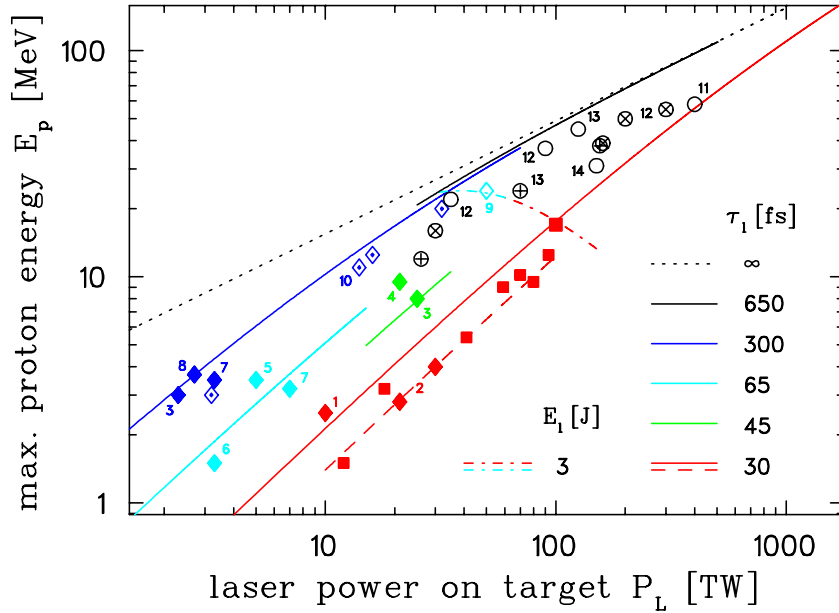


Figure 4. Scaling of the maximum proton energy with laser power. Red squares represent experimental results obtained with the Draco laser by varying the laser energy between 0.3 and 3 J (small squares: $d = 5 \mu\text{m}$ target thickness, big square: $d = 2 \mu\text{m}$). Filled diamonds stand for experiments performed with Ti:sapphire lasers of around 1 J energy (1: Lund [17], 2: J-Karen [18, 19], 3: MBI [9, 20], 4: LOA [21], 5: Saclay [22], 6: Astra [23], 7: Jeti [24], 8: Atlas [25]), partially (3,7) operated at a longer pulse length than usual. The open diamond (9) represents a 5 J experiment at Janusp [26], and the dotted diamonds (10) show the results of an energy scan applying up to 10 J on the target and at LULI [8]. Open circles (11,12,13,14) stand for single shot experiments at the glass laser facilities LLNL NovaPW [27], RAL Vulcan [28], Los Alamos Trident [29, 30] and Phelix GSI [6]. Marked circles represent recent energy scans ranging up to 300 J performed at Vulcan and Trident [29, 31]. The color code of the experimental points corresponds to the different pulse duration regimes given in the legend for the curves following equation (3). Representative sets of parameters are chosen for $(r_1 (\mu\text{m}), d (\mu\text{m}) \text{ and } \vartheta (^{\circ}))$, i.e. (1.7–2.3, 2, 10) for $\tau_1 = 30\text{--}65$ fs with the exception of the dashed red line where $d = 5 \mu\text{m}$, (3, 15, 15) for $\tau_1 = 300$ fs and (5, 15, 30) for $\tau_1 > 500$ fs. The efficiency η is set to $\eta = 0.2$, matching the short-pulse case, and is kept constant as described in the text.

charge $Q = 2N_e(\zeta_t R)/(\tau_1 c)$ allows for the rewriting of the potential barrier $E_\infty = Qe^2/(2\pi\epsilon_0 R)$ in equation (1) as a function of the laser power $P_1 = E_1/\tau_1$

$$E_\infty = 2m_e c^2 \sqrt{\frac{\eta P_1}{P_e}} \quad (2)$$

using the relativistic power unit $P_e = m_e c^3/r_e = 8.7$ GW. Up to this point, no assumption has been required about the energy distribution of the hot electrons. Nevertheless, when applying an exponential distribution with $E_e = k_B T_e$, the turning point of electrons with E_e running up

the potential corresponds to the hot electron Debye length λ_D and the surface field is consistent with the one resulting from the established plasma expansion model [10].

The energy of a laser-accelerated proton is now deduced from the potential caused by the induced surface charge at the actual position of the proton ζ to $E_p(\zeta) = -e\Phi(r=0, \zeta) = -E_\infty(1 + \zeta - \sqrt{1 + \zeta^2})$. The size of the surface charge thus influences the energy gain of protons close to the surface ($\zeta = z/R < 1$). For a quantitative analysis of the maximum energy E_{\max} that a proton can reach, integration of the equation of motion up to the duration of the laser pulse leads to an implicit function [9] that can be approximated by

$$\begin{aligned} E_{\max} &= E_\infty \tanh^2\left(\frac{\tau_1}{2\tau_0}\right) \\ &\rightarrow E_\infty \left(\frac{\tau_1}{2\tau_0}\right)^2 \propto \eta P_1 \quad \text{for } \tau_1 \ll 2\tau_0 \\ &\rightarrow E_\infty \propto \sqrt{\eta P_1} \quad \text{for } \tau_1 \gg 2\tau_0. \end{aligned} \quad (3)$$

The reference time $\tau_0 = R/v_\infty = R/(2E_\infty/m_p)^{1/2}$ is used to emphasize the time the proton remains in the vicinity of the accelerating surface charge. It directly follows that for acceleration times and thus pulse durations shorter than twice the reference time τ_0 , the scaling of the maximum proton energy with laser power is dominantly linear. This situation applies for the Draco data presented in figure 4, where for $P_1 \sim 100$ TW the reference time amounts to $\tau_0 \sim 20$ fs and the pulse duration to $\tau_1 = 30$ fs. Using the measured focal radius of $r_1 = 1.7 \mu\text{m}$ and a well-established propagation angle of $\vartheta = 10^\circ$, and assuming a conversion efficiency of $\eta = 20\%$, our experimental data are well described by equation (3), where the red solid line in figure 4 corresponds to a target thickness of $d = 2 \mu\text{m}$ and the dashed line to $d = 5 \mu\text{m}$. A set of solid curves is additionally displayed for slightly longer (color-coded) pulse durations to guide the eye.

For higher powers of ultrashort pulses, the influence of the source size diminishes as the reference time τ_0 decreases, leading to the curvature of the red line. The same holds true for longer laser pulses, thus increasing acceleration times. For all cases the scaling converges to the square-root scaling for $\tau_1 \gg 2\tau_0$. The corresponding dotted line in figure 4 therefore represents an upper limit of the proton energy for a given laser power, provided that the conversion efficiency is assumed to be constant. As it is not the intention of this paper to discuss the absolute proton energies achievable with long pulse lasers, but only the scaling behavior in relation to the short pulse case, the increase of the absorption efficiency to up to 50% [8], being well established for this laser class, has been ignored in all the curves of figure 4.

We are aware of the fact that the model strongly simplifies the acceleration dynamics, especially with regard to the 1D plasma expansion model [8, 10]. However, as it has been successfully used to describe maximum energies and pulse duration dependencies in the past and nicely describes the principle behavior of our experimental findings, we feel that it can be used to discuss the efficiency of modern ultrashort pulse laser systems for proton acceleration. Keeping for the present discussion conversion efficiency and electron divergence constant, optimum use of the laser power can be made when $(\tau_1/\tau_0) \sim 2.5$ [32], which for the Draco parameters discussed here would correspond to $P_1 \sim 1$ PW. It thus turns out (red curve in figure 4) that ultrashort laser pulses can be efficiently used for the acceleration of protons in the TNSA regime when (a) the laser pulse is focused tightly and (b) the laser power is well above a few 100 TW. For the laser energies at present available at Draco (3–4 J), optimum conditions

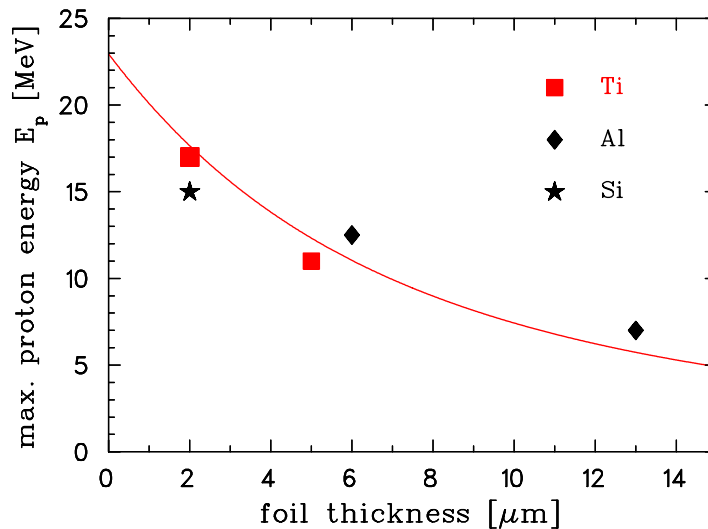


Figure 5. Maximum proton energy as a function of the thickness of the given target material. The red line follows equation (3) for a fixed laser power of $P_1 = 100$ TW, a focal radius of $r_1 = 1.7 \mu\text{m}$ and $\vartheta = 10^\circ$.

should accordingly exist for somewhat longer pulses (dash-dotted line in the figure) of about $\tau_1 = 75$ fs.

As electrons are believed to penetrate the target foil with a divergence angle $\vartheta \sim 10^\circ$, maintaining condition (a), i.e. a small source size at the target rear, not only requires tight focusing but also thin foils of the order of $d \sim 1 \mu\text{m}$. However, as discussed in the following section, at a laser power level of 100 TW, excellent pulse contrast is required to be able to take advantage of such foil thicknesses. Figure 5 shows maximum proton energies as a function of the foil thickness and the foil material for nearly identical laser parameters. Again, the general trend can be nicely reproduced by the red line in the figure representing the Schreiber model (equation (3)) for the same parameters that are used in figure 4. Furthermore, no significant changes are observed at the 100 TW level when different target materials are used. Especially for the case of the semiconductor silicon, this finding allows for a more complex target design based on straightforward wafer preparation technologies.

4. Proton acceleration from foil targets distorted by shock waves

Although Thomson parabola spectrometers provide an excellent energy resolution, absolute proton numbers as well as the energy-dependent beam divergence above about 1 MeV can be best determined with stacked RCF films. As this information is of particular importance for the design of beam transport systems and thus for most applications, images of representative shots were recorded. In these shots, a systematic deviation of the emission angle of the most energetic protons from the target normal was found for the 2- μm -thick foil targets, as illustrated by the raw RCF images presented in figure 3. Consequently, in these shots, the small acceptance angle of the online spectrometer did not cover the full energy range.

For two characteristic shots on foils of different thicknesses (2 and 5 μm titanium foil), this deflection is analyzed in figure 6. The centroid derived from the angular distribution is plotted for proton energies corresponding to the stopping power in the particular RCF stack layers as

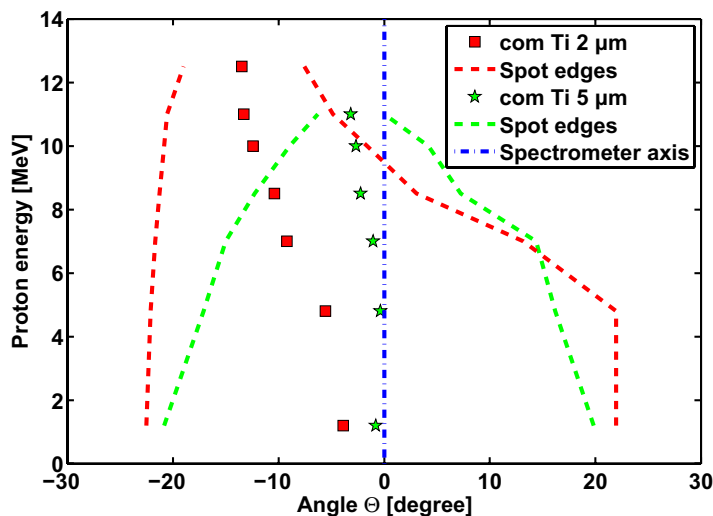


Figure 6. Deviation of the proton emission toward the laser axis with respect to the global target normal direction at $\theta = 0^\circ$. For different foil thicknesses, the centroid (com) of the angular distribution (horizontal cut) is plotted as well as the edges of the spot, representing the maximum divergence of the corresponding energy class.

a function of the deflection angle θ , where $\theta = 0^\circ$ marks the target normal and thus the online spectrometer axis. With increasing proton energy the emission is found to be shifted by up to 15° from the target normal toward the direction given by the laser axis ($\theta = -45^\circ$). For the thicker target the effect is considerably reduced.

Dashed lines indicate the corresponding spot edges in the horizontal cut of the angular proton emission distribution. The edges illustrate an energy-dependent beam divergence of the order of 10° – 20° , which is slightly reduced for thicker foils, as well. For a set of more than 30 consecutive shots, this behavior was reproduced with the deflection of the most energetic protons exhibiting a fluctuation of about $\pm 5^\circ$.

This general behavior also holds true when the angle of incidence ϕ (or the foil orientation, respectively) is slightly rotated, allowing for the optimization of the online detection system. For such an optimized angle, higher proton energies, consistent with the RCF stack measurements, are recorded (not explicitly shown). Further, for this condition, only highest carbon and oxygen ion charge states are observed in the Thomson parabola spectrometer.

These findings can be explained by a scheme first discussed by the group at the Lund laser facility in 2005 [13, 33]. The ns ASE pedestal of an ultrashort laser pulse with sufficient intensity ($\approx 10^{12} \text{ W cm}^{-2}$) can form a preplasma at the front surface of the target. As the preplasma expands into vacuum, it launches a cold and plastic shock wave with a velocity of the order of $\mu\text{m ns}^{-1}$. The shock front breaks through the rear surface of the foil and results in a significant deformation (several μm) of this surface (sketched in the left part of figure 7). As long as the rear surface remains intact and the ion density gradient remains steep, effective proton acceleration in the TNSA scheme occurs during the time the ultrashort laser pulse is interacting with the target foil. At higher ASE intensities, the maximum proton energy can be limited due to a longer plasma scale length [25, 34]. The deformed target geometry finally determines the emission direction of the energetic proton pulse. When the main laser pulse impinges on

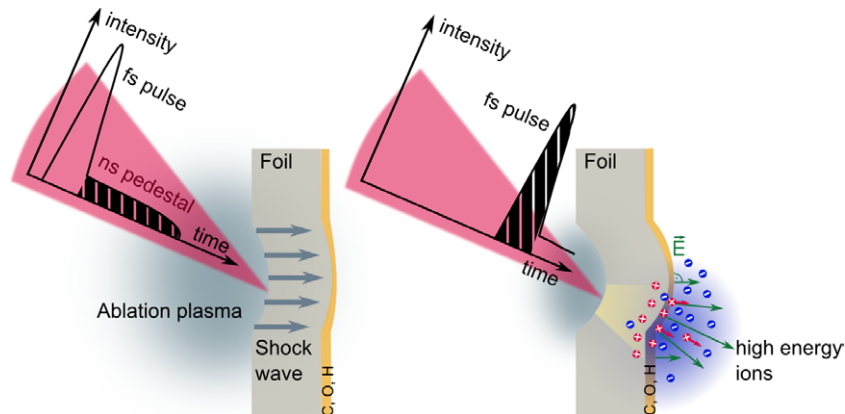


Figure 7. Schematic overview of the proton acceleration from a foil target after shock wave deformation. (Left) An ASE pedestal with a duration of a few ns generates a cold ablation plasma, which expands and launches a shock wave into the target foil. The shock front breaks through and deforms the rear surface while the plasma scale length remains small. (Right) The main part of the ultrashort laser pulse interacts with the deformed foil at oblique incidence, generating hot electrons, which are asymmetrically distributed at the rear surface. The most energetic protons stem from a small area with a local target normal shifted toward the laser axis. Protons with less energy originate from a larger area with an average target normal more parallel to the global target normal.

the target, electrons are asymmetrically distributed along the target rear surface (sketched in the right part of figure 7). At the position where the laser hits the deformed target, the highest field gradients are created. Hydrogen and heavier ions are completely field ionized and protons are accelerated to the highest energies. Protons originating from this area are steered toward the laser axis ($\theta < 0^\circ$) according to the local deformation. Since lower energetic protons stem from a larger region, they experience on average less deflection, as can be seen in figure 6. Less deformation, and hence less deflection, is also expected for the thicker target foils. Moreover, the magnitude of the rear side deformation influences the divergence of the proton emission, which is reduced for the thicker target in figure 6, as well.

4.1. Modeling of the target deformation

In order to model the shape of the target deformation, we apply a simple analytical model, which employs the quasi-two-dimensional scheme presented by Lundh *et al* in [13] for the characterization of the shock wave ballistics. The deformation amplitude depends on the velocity of the shock front v_s driving through the target and the deformation velocity v_d of the target rear surface after shock break-through. From mass and momentum conservation, $v_s = c_0(\sqrt{1+x}+1)/2$ and $v_d = c_0(\sqrt{1+x}-1)/\alpha$ are derived. Here the parameter x equals $x = (4\alpha/\rho_0 c_0^2)I^{2/3}$, where I is the ASE intensity of the laser, ρ_0 the density, c_0 the speed of sound and α a material-specific parameter. For our experimental conditions ($I = 5 \times 10^{12} \text{ W cm}^{-2}$, Ti foil with $\rho_0 = 4.53 \text{ g cm}^{-3}$, $c_0 = 5.24 \text{ } \mu\text{m ns}^{-1}$, $\alpha = 1.02$ and $d = 2 \text{ } \mu\text{m}$), $v_s = 7.8 \text{ } \mu\text{m ns}^{-1}$ and $v_d = 5.7 \text{ } \mu\text{m ns}^{-1}$ can be derived. For an estimated ASE duration of $\tau_{\text{ASE}} = 1.8 \text{ ns}$, we obtain a

Table 2. Comparison of the ASE intensities in different experiments (for Draco taking a contrast ratio of 5×10^{-9}) and of the corresponding shock velocities derived following Lundh *et al* and the experiment of Kaluza *et al*.

	ASE intensity (W cm ⁻²)	Shock velocity $v_s(v_d)$ ($\mu\text{m ns}^{-1}$)		τ_{ASE} (ns)
		Al	Ti	
Lundh <i>et al</i>	2×10^{12}	9 (5)	6.7 (3.6)	1–2
Kaluza <i>et al</i>	5×10^{11}	>3.6		0.5–2.5
Draco	5×10^{12}		7.8 (5.7)	1.5–2

maximum displacement of the target rear surface from its initial position of $v_d(\tau_{\text{ASE}} - d/v_s) = 9 \mu\text{m}$. In table 2, the model parameters for the latter velocities are compared to the results from Kaluza *et al* [25], where the velocity of the perturbation front is estimated from the dependence of the optimum thickness on the prepulse duration. Although the ASE intensity at this experiment is considerably lower than for the present case, this velocity is of the same magnitude as the shock velocities derived with the model. This confirms that even for very thin foils of only $2 \mu\text{m}$, which turned out to be the optimal thickness for the 100 TW Draco laser parameters, the target rear surface remains intact, although the calculated deformation is larger than the foil thickness.

We further assume that the angular distribution of the emitted protons follows the shape of the generated Debye sheath [1]. The protons start perpendicular to the target surface and, in this picture, are subsequently deflected to pass perpendicular to the isosurface of the Debye sheath. The sheath is thus modeled as a superposition of a Gaussian-shaped target foil $f(x) = A \exp(-x^2/2\sigma^2)$ and a different Gaussian sheath in a static situation and the angular distribution calculated accordingly (see figure 8 (top)).

The width of the Gaussian target shape 2σ can be fixed for the given deformation amplitude A using the experimental observable of the maximum deflection angle $\theta = 14^\circ$ of the centroids (figure 6), assuming that the most energetic protons originate from the point on the foil where the laser pulse is arriving at the deformed target.

Taking $\tan \phi = f(x)/x$ and $\tan \theta$ as the derivation of $f(x)$, this leads to the relation $\sigma = A/\sqrt{\tan \phi \tan \theta \exp(\tan \theta / \tan \phi)} = 16 \mu\text{m}$. The maximum of the Gaussian-shaped plasma sheath is set to the same position. A sheath amplitude of $1 \mu\text{m}$ (typical Debye length of the order of a wavelength) is used and the width of $9 \mu\text{m}$ is adjusted to match the maximum emission angles observed on the RCF stack layers. Angular proton distributions are evaluated corresponding to different sizes of proton sources and their centroid is determined and compared to the measured data, as depicted in the lower panel of figure 8. The shape of the model curve fits the RCF stack data surprisingly well. Although from this model the target shape cannot be predicted unambiguously because neither temporal plasma sheath evolution nor realistic field gradients are included, the proton source sizes for individual energy classes can be deduced indirectly. For a target thickness of $d = 2 \mu\text{m}$, a laser focal spot radius of $r_L = 1.6 \mu\text{m}$ and a half opening angle of the hot electron spread in the foil of $\vartheta = 10^\circ$, the source size of the most energetic protons can be estimated as $2(r_L + d \tan \theta) = 4 \mu\text{m}$. This compares well to the model prediction (see figure 8). The obtained linear dependence between source size and proton energy reproduces the tendency published in [35] where the source size is measured with foil targets with microgrooved rear side.

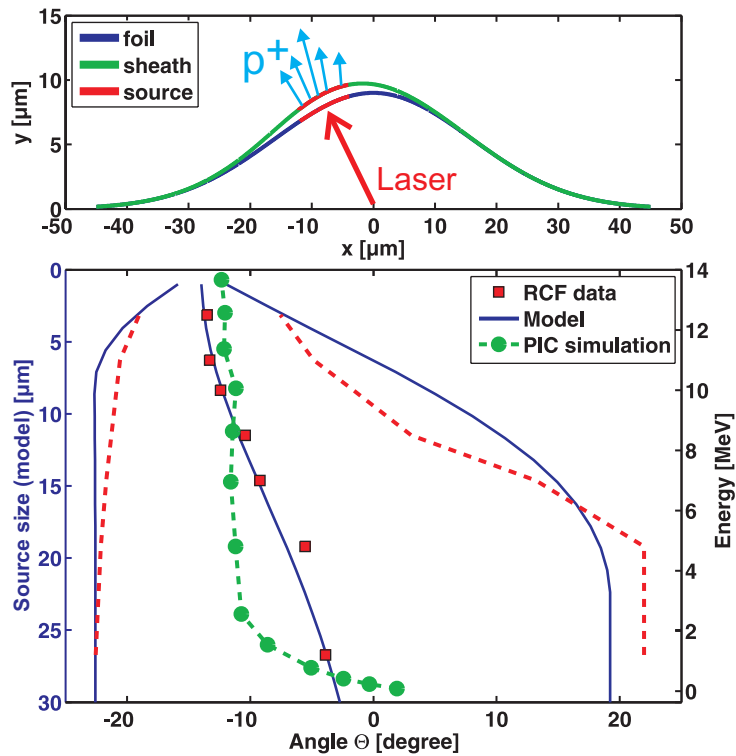


Figure 8. (Top) Schematic representation of the model used to describe the foil deformation for the Draco parameters. The laser pulse impinges under 45° on the target, treated as the superposition of a Gaussian-shaped foil and a Gaussian-shaped Debye sheath with the maximum shifted to the interaction position. Distributions of the proton emission angles are calculated for different source sizes, corresponding to different intervals of the sheath curve (marked red in the upper figure). (Bottom) For varying source sizes the centroid (com) of the individual angular distributions is calculated and correlated with the same data obtained by the RCF stack measurement as in figure 6. Independently, the com of the proton emission distributions obtained from a 2D PIC simulation as a function of the proton energy is included.

4.2. Particle-in-cell (PIC) simulation

In order to validate the simplified treatment of the sheath in the previous discussion, the interaction of the main pulse with the same predeformed target is simulated using the 2D PIC code PICLS [36]. The simulation box was set to $200 \mu\text{m} \times 200 \mu\text{m}$ with 79 cells per micron. To save computation time, the electron density of the titanium foil is reduced to $100 n_c$, starting with a fully preionized neutral plasma of $1 \mu\text{m}$ titanium ions covered with a 50 nm proton layer at the rear surface. For the target deformation due to the ASE, we assume a similar Gaussian shape of $35 \mu\text{m}$ width at FWHM and $9 \mu\text{m}$ amplitude. Figure 9(d) shows the ion charge density profile before the main laser pulse hits the target. The laser pulse, having a Gaussian spatial and temporal profile with a waist of $7 \mu\text{m}$ and duration of 30 fs at FWHM, enters the simulation box from the left at 45° with respect to the target. The laser is focused to the center of the Gaussian; hence it hits the deformed target off-center, see figure 9(a).

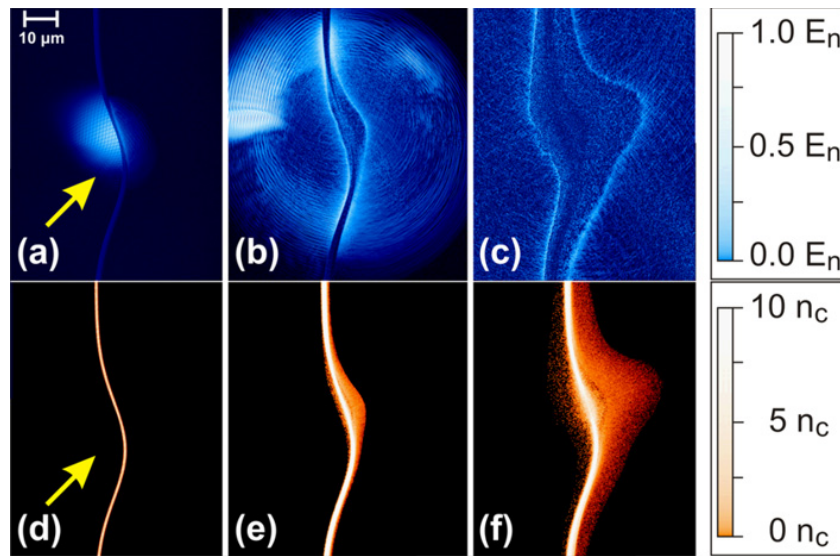


Figure 9. Simulated electric field strength ((a)–(c)) (normalized to $E_a = 10E_0$ (a), $E_b = 1E_0$ (b) and $E_c = 0.1E_0$ (c)) and ion charge density distribution ((d)–(f)) at the time the laser pulse maximum hits the target ((a) and (d)) and 100 fs ((b) and (e)) and 335 fs ((c) and (f)) later. (a) The laser main pulse is seen to hit the target at 45° incidence (yellow arrow), being partly reflected. ((b) and (c)) The reflected pulse leaves the simulation box to the left, while the electron Debye sheath creates an electric field at the front and rear target surface. This sheath field is not symmetric, leading to asymmetric acceleration of ions ((e) and (f)), with the fastest ions shifted toward the laser direction. The low-energy protons are stemming from the distant wings where the target preformation, and hence sheath asymmetry, is negligible.

Figure 9 shows the temporal evolution of the electric field strength ((a)–(c)) and ion charge density ((d)–(f)). It is seen that the laser hitting the target off-center (a) indeed creates an asymmetric electric field distribution ((b) and (c)). The Debye sheath tip is seen to move normal to the predeformed target surface at the location where the laser hits. As this is where the high-energy ions originate from, they are also moving in that direction ((d)–(f)).

Similar to the previous analytical discussion, the centroid of the angular proton emission distribution for different proton energies is evaluated and included in figure 8. Although the exact curvature does not reproduce the recorded data perfectly, in the PIC simulation the deflection angle for the most energetic ions is reproduced. Thus, the PIC simulation that considers the temporal plasma expansion also supports the assumption that the shape of the target foil is indeed imprinted in the shape of the field gradients.

5. Conclusions

In summary, it was possible to demonstrate that with state-of-the-art 100 TW class ultrashort pulse lasers and micron-thick foil targets, proton pulses can be effectively accelerated to energies up to 17 MeV in the established TNSA regime. The observed linear scaling with laser power

suggests that already with 500 TW class lasers, the present maximum proton energy limit of about 50 MeV reached with high-energy lasers could be realized. Only plain foil targets and non-destructive laser pulse cleaning techniques (i.e. no plasma mirrors) were used, so that for the first time applications making use of full 10 Hz operation can be envisioned. In principle, the approach can be extended also to micro-coated dot targets, demonstrated to narrow the energy bandwidth at low energies [11]. Small deflections of the proton pulses induced by target deformation in the remaining ASE level were observed and investigated because of their importance for the determination of the proton energy scaling. The target deformation was shown to be predictable by analytical modeling as well as PIC simulations. They appear stable and may potentially be included in the design of proton beam delivery optics.

Above an energy level of 4 MeV, a laser to proton energy conversion efficiency of about 0.5% could be deduced from RCF stack measurements (i.e. a proton pulse energy of 6 mJ), whereas for energies above 10 MeV a typical dose of 2.5 Gy was detected on an area of a few square centimeters. Thus, systematic radiobiological experiments, requiring radiation doses of an order of one to tens of Gy at short irradiation times on minute scales, are well within reach.

Although TNSA scaling laws appear to be well investigated, for ultrashort pulses and intensities in the range of $10^{21} \text{ W cm}^{-2}$ it is seen that more detailed experimental studies are required. For a full understanding of the achievable proton and ion energies, this would include further study of laser absorption, and interferometric studies of the extension of the sheath field, especially when extended to TNSA regimes [37] where submicron-thick target foils start to become transparent.

References

- [1] Cowan T E *et al* 2004 Ultralow emittance, multi-MeV proton beams from a laser virtual-cathode plasma accelerator *Phys. Rev. Lett.* **92** 204801
- [2] Li C K *et al* 2006 Measuring E and B fields in laser-produced plasmas with monoenergetic proton radiography *Phys. Rev. Lett.* **97** 135003
- [3] Romagnani L *et al* 2005 Dynamics of electric fields driving the laser acceleration of multi-MeV protons *Phys. Rev. Lett.* **95** 195001
- [4] Nickles P V, Schnürer M, Sokollik T, Ter-Avetisyan S, Sandner W, Amin M, Toncian T, Willi O and Andreev A 2008 Ultrafast laser-driven proton sources and dynamic proton imaging *J. Opt. Soc. Am. B* **25** B155
- [5] Nakamura S *et al* 2007 High-quality laser-produced proton beam realized by the application of a synchronous electric RF field *Japan J. Appl. Phys.* **46** L717
- [6] Roth M 2009 private communication
- [7] Ledingham K W D, Galster W and Sauerbrey R 2007 Laser-driven proton oncology a unique new cancer therapy? *Br. J. Radiol.* **80** 855
- [8] Fuchs J *et al* 2006 Laser-driven proton scaling laws and new paths towards energy increase *Nat. Phys.* **2** 48
- [9] Schreiber J *et al* 2006 Analytical model for ion acceleration by high-intensity laser pulses *Phys. Rev. Lett.* **97** 045005
- [10] Mora P 2003 Plasma expansion into a vacuum *Phys. Rev. Lett.* **90** 185002
- [11] Schwoerer H, Pfothner S, Jackel O, Amthor K-U, Liesfeld B, Ziegler W, Sauerbrey R, Ledingham K W D and Esirkepov T 2006 Laser-plasma acceleration of quasi-monoenergetic protons from microstructured targets *Nature* **439** 445
- [12] Psikal J, Tikhonchuk V T, Limpouch J, Andreev A A and Brantov A V 2008 Ion acceleration by femtosecond laser pulses in small multispecies targets *Phys. Plasmas* **15** 053102

- [13] Lundh O, Lindau F, Persson A, Wahlström C G, McKenna P and Batani D 2007 Influence of shock waves on laser-driven proton acceleration *Phys. Rev. E* **76** 26404
- [14] Amplitude Technologies 2009 <http://www.amplitude-technologies.com/>
- [15] Pretzler G, Kasper A and Witte K J 2000 Angular chirp and tilted light pulses in CPA lasers *Appl. Phys. B* **70** 1
- [16] Nürnberg F *et al* 2009 Radiochromic film imaging spectroscopy of laser-accelerated proton beams *Rev. Sci. Instrum.* **80** 033301
- [17] Neely D, Foster P, Robinson A, Lindau F, Lundh O, Persson A A, Wahlström C-G and McKenna P 2006 Enhanced proton beams from ultrathin targets driven by high contrast laser pulses *Appl. Phys. Lett.* **89** 021502
- [18] Pirozhkov A S *et al* 2009 Laser-driven proton acceleration and plasma diagnostics with J-KAREN laser *Proc. SPIE* **7354** 735414
- [19] Nishiuchi M *et al* 2009 Focusing and spectral enhancement of a repetition-rated, laser-driven, divergent multi-MeV proton beam using permanent quadrupole magnets *Appl. Phys. Lett.* **94** 061107
- [20] Steinke S and Sokollik T 2009 private communication
- [21] Fritzier S, Malka V, Grillon G, Rousseau J P, Burgy F, Lefebvre E, d'Humieres E, McKenna P and Ledingham K W D 2003 Proton beams generated with high-intensity lasers: applications to medical isotope production *Appl. Phys. Lett.* **83** 3039
- [22] Ceccotti T, Lévy A, Popescu H, Réau F, D'Oliveira P, Monot P, Geindre J P, Lefebvre Ph and Martin E 2007 Proton acceleration with high-intensity ultrahigh-contrast laser pulses *Phys. Rev. Lett.* **99** 185002
- [23] Spencer I *et al* 2003 Experimental study of proton emission from 60-fs, 200-mJ high-repetition-rate tabletop-laser pulses interacting with solid targets *Phys. Rev. E* **67** 046402
- [24] Jäckel O 2009 Characterization of ion acceleration with relativistic laser pulses *PhD Thesis* FSU Jena
- [25] Kaluza M, Schreiber J, Santala M I K, Tsakiris G, Eidmann K, Meyer-ter Vehn J and Witte K 2004 Influence of the laser prepulse on proton acceleration in thin-foil experiments *Phys. Rev. Lett.* **93** 045003
- [26] Mackinnon A J, Sentoku Y, Patel P K, Price D W, Hatchett S, Key M H, Andersen C, Snavely R and Freeman R R 2002 Enhancement of proton acceleration by hot-electron recirculation in thin foils irradiated by ultraintense laser pulses *Phys. Rev. Lett.* **88** 215006
- [27] Snavely R A *et al* 2000 Intense high-energy proton beams from petawatt-laser irradiation of solids *Phys. Rev. Lett.* **85** 2945
- [28] Zepf M *et al* 2001 Fast particle generation and energy transport in laser-solid interactions *Phys. Plasmas* **8** 2323
- [29] Flippo K A, Workman J, Gautier D C, Letzring S, Johnson R P and Shimada T 2008 Scaling laws for energetic ions from the commissioning of the new Los Alamos National Laboratory 200 TW Trident laser *Rev. Sci. Instrum.* **79** 10E534
- [30] Gaillard S and Flippo K A 2009 private communication
- [31] Robson L *et al* 2006 Scaling of proton acceleration driven by petawatt-laser-plasma interactions *Nat. Phys.* **3** 58
- [32] Schreiber J 2009 Towards relativistic laser ion acceleration unpublished
- [33] Lindau F, Lundh O, Persson A, McKenna P, Osvay K, Batani D and Wahlström C G 2005 Laser-accelerated protons with energy-dependent beam direction *Phys. Rev. Lett.* **95** 175002
- [34] Mackinnon A J, Borghesi M, Hatchett S, Key M H, Patel P K, Campbell H, Schiavi A, Snavely R, Wilks S C and Willi O 2001 Effect of plasma scale length on multi-MeV proton production by intense laser pulses *Phys. Rev. Lett.* **86** 1769
- [35] Schollmeier M *et al* 2008 Laser beam-profile impression and target thickness impact on laser-accelerated protons *Phys. Plasmas* **15** 053101
- [36] Sentoku Y and Kemp A J 2008 Numerical methods for particle simulations at extreme densities and temperatures: weighted particles, relativistic collisions and reduced currents *J. Comput. Phys.* **227** 6846
- [37] d'Humières E, Lefebvre E, Gremillet L and Malka V 2005 Proton acceleration mechanisms in high-intensity laser interaction with thin foils *Phys. Plasmas* **12** 062704